JACS
JOURNAL OF THE AMERICAN CHEMICAL SOCIETY
pubs.acs.org/JACS
Article

Structured-Liquid Batteries

Jiajun Yan, Michael A. Baird, Derek C. Popple, Alex Zettl, Thomas P. Russell, and Brett A. Helms*

Cite This: J. Am. Chem. Soc. 2022, 144, 3979−3988
Read Online
ACCESS | Metrics & More | Article Recommendations | Supporting Information

ABSTRACT: Chemical systems may be maintained far from equilibrium by sequestering otherwise reactive species into different microenvironments. It remains a significant challenge to control the amount of chemical energy stored in such systems and to utilize it on demand to perform useful work. Here, we show that redox-active molecules compartmentalized in multiphasic structured-liquid devices can be charged and discharged to power a load on an external circuit. The two liquid phases of these devices feature charge-complementary polyelectrolytes that serve a dual purpose: they generate an ionically conductive coacervate membrane at the liquid−liquid interface, providing structural support; they also mitigate active-material crossover between phases via ion pairing with the oppositely charged anolyte and catholyte active materials. Structured-liquid batteries enabled by this design were rechargeable over hundreds of hours. We envision that these devices may be integrated with soft electronics to enable functional circuits for smart textiles, medical implants, and wearables.

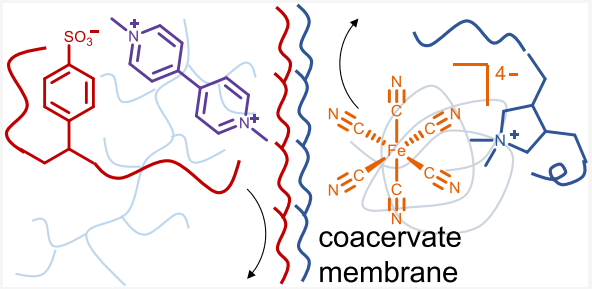

Downloaded via UNIV OF CALIFORNIA BERKELEY on August 3, 2022 at 23:26:46 (UTC).
See https://pubs.acs.org/sharingguidelines for options on how to legitimately share published articles.

INTRODUCTION

All-liquid batteries show tremendous versatility in form and function with the potential to power energy systems as large as the grid and as small as a wearable device. The cell chemistry for these batteries most often features high-temperature molten liquid metals,[1,2] low-temperature eutectic alloys,[3−6] or solutions of redox-active compounds.[7−9] Notably, due to the conformal character of liquids, both negative and positive electrodes adopt the shape of their container, sometimes through the aid of a physical separator, or membrane, although membrane-less designs are also possible.[10−14]

An emerging strategy for the creation of all-liquid devices makes use of load-bearing interfacial assemblies of polymers or nanoparticles to structure liquids into prescribed shapes such that formal containment is no longer necessary.[15−20] Structured liquids can be patterned and printed from a broad palette of liquid media, both aqueous and nonaqueous. The membrane between the liquid phases has selective transport properties, depending on the components from which it is assembled.[17,19] To apply this strategy to the fabrication of structured-liquid batteries requires that the negative and positive electrodes be loaded with not only charge-storing active materials but also components that assemble into a membrane at the liquid−liquid interface—both to support the structure of the patterned or printed all-liquid system, as well as to provide a conduit for ionic charge when the device is charged and discharged upon application of an electrochemical potential. Additional considerations arise from the need to sequester charge-storing active materials in each of the liquid phases serving as anolytes or catholytes in the device.

Here, we harness the interfacial assembly of polyelectrolytes to fabricate structured-liquid batteries on hydrophobic substrates with patterned hydrophilic electrodes (Figure 1).[19] By controlling the geometry and surface chemistry of current collectors,[21,22] we can prescribe an interface between aqueous biphasic anolytes and catholytes deposited onto the electrodes (Figure 1B). Once the interface is formed, polyanions, e.g., poly(sodium 4-styrenesulfonate), PSS−Na, dissolved in the anolyte form an ionically conductive coacervate membrane with polycations, e.g., poly(diallyldimethylammonium chloride), PDADMA−Cl, dissolved in the catholyte.[19,23] We also leverage ion pairing between polyelectrolytes and oppositely charged charged active materials to mitigate the rate of active-material crossover between phases, allowing the device to be cycled over hundreds of hours.[24−26] The power delivered by such devices is on the order of that found in biological circuits and sensors, demarking future use—cases based on that complementarity.

Received: November 24, 2021
Published: February 23, 2022

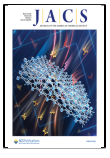

ACS Publications
© 2022 American Chemical Society

https://doi.org/10.1021/jacs.1c12417
J. Am. Chem. Soc. 2022, 144, 3979−3988

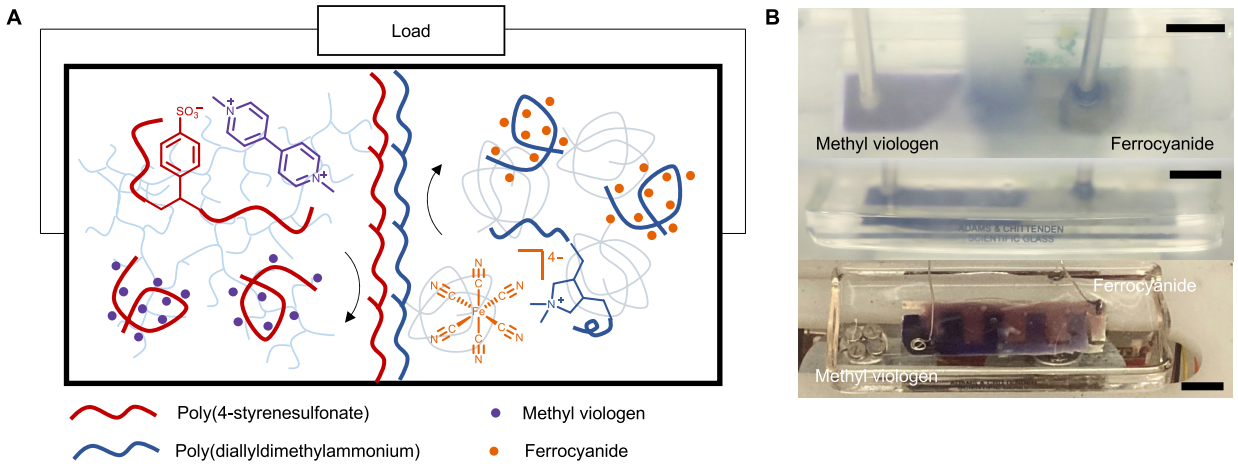

Figure 1. (A) Structured-liquid batteries are fabricated from all-aqueous biphasic liquid electrode-based solutions of dextran and PEG. Here, the dextran-rich phase (light blue) also comprised methyl viologen (purple dots) and PSS−Na, a polyanion (red coils). The PEG-rich phase (light orange) also comprised ferrocyanide (orange dots) and PDADMA−Cl, a polycation (blue coils). From PSS−Na and PDADMA−Cl, a membrane self-forms at the interface between the electrodes. (B) Photographs of the all-aqueous biphasic electrochemical cell during cycling. The dextran-rich phase turns dark blue on charge, confirming the presence of the methyl viologen radical cation. The brown color in the PEG-rich phase results from a reaction between methyl viologen and ferrocyanide tied to crossover. Scale bars: 1 cm.

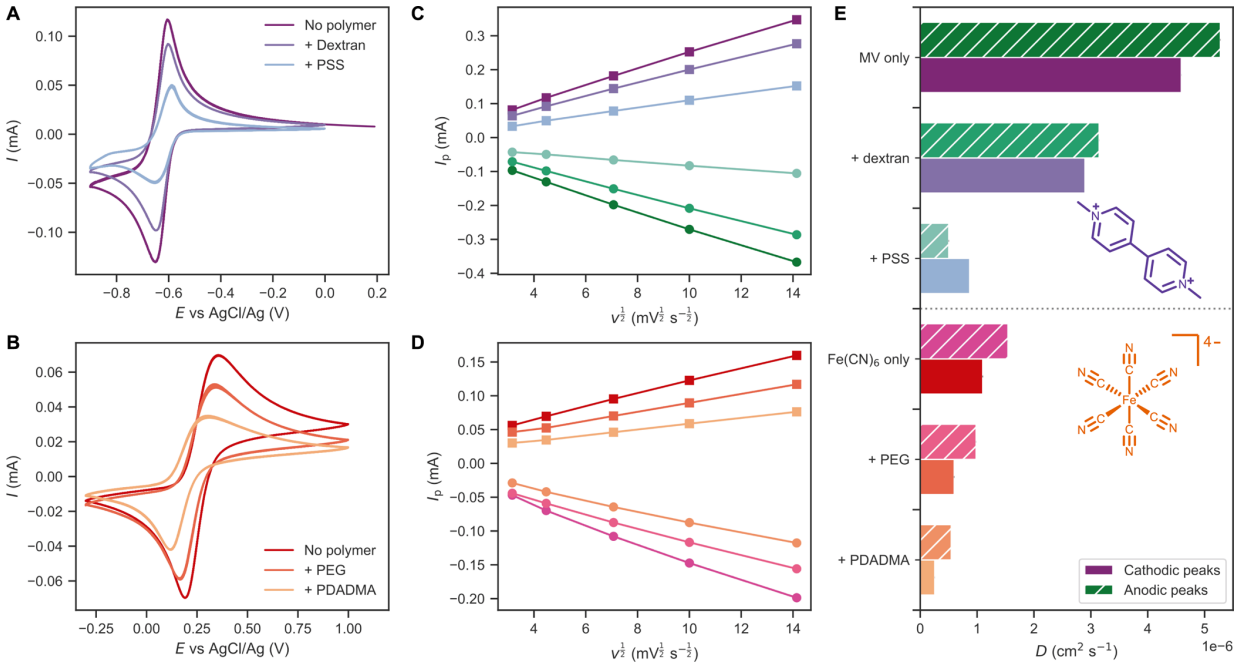

Figure 2. (A) Cyclic voltammetry of 10 mg mL^{-1} methyl viologen without polymers, in 15% dextran, or in 15% dextran and 1% PSS at 20 mV s^{-1}. (B) Cyclic voltammetry of 10 mg mL^{-1} ferrocyanide without polymers, in 10% PEG, or in 10% PEG and 1% PDADMA at 20 mV s^{-1}. (C) Randles−Sevcik plot of the cathodic and anodic peak currents of methyl viologen. (D) Randles−Sevcik plot of the cathodic and anodic peak currents of ferrocyanide. (E) Diffusion coefficients, calculated using ordinary least-squares linear regression, and half-peak potentials of the redox-active species, with or without the polymers. Cyclic voltammetry performed using a 3 mm glassy carbon working electrode, a 3.0 M NaCl AgCl/Ag reference electrode, and a Pt counter electrode.

RESULTS AND DISCUSSION

Electrolyte Design. For anolyte and catholyte phases in the device, we used an aqueous two-phase system (ATPS) comprising dextran in one of the phases and poly(ethylene glycol) (PEG) in the other.[27−29] As active materials, we used a cationic methyl viologen (−0.45 V vs standard hydrogen electrode (SHE)) for the anolyte and an anionic ferrocyanide (0.44 V vs SHE) for the catholyte. On reduction, methyl viologen is a radical cation; on oxidation, ferrocyanide changes oxidation state yet remains anionic. Each active material is well-behaved and variants of both with different supporting salts control their solubility and reversibility in aqueous electrolytes.[30−33] Counterions are known to influence the

https://doi.org/10.1021/jacs.1c12417
J. Am. Chem. Soc. 2022, 144, 3979−3988

Table 1. Electrochemical and Transport Properties of Liquid Electrolytes

active species	medium	$E_{p/2}$ (V vs AgCl/Ag)[a]	D_c (cm^2 s^{-1})[b]	D_a (cm^2 s^{-1})[b]	η (cSt)[c]	R (Ω)[d]
MV^{2+}	NH_4Cl	−0.612 ± 0.001	(4.59 ± 0.01) × 10^{-6}	(5.28 ± 0.01) × 10^{-6}	1.07 ± 0.02	81.9 ± 0.2
	NH_4Cl + dextran	−0.609 ± 0.001	(2.90 ± 0.01) × 10^{-6}	(3.15 ± 0.01) × 10^{-6}	65.5 ± 0.7	103.4 ± 0.3
	NH_4Cl + dextran + PSS	−0.599 ± 0.002	(8.68 ± 0.01) × 10^{-7}	(5.03 ± 0.04) × 10^{-7}	65.5 ± 1.8	101.8 ±0.3
$Fe(CN)_6^{4-}$	NH_4Cl	0.249 ± 0.001	(1.10 ± 0.01) × 10^{-6}	(1.54 ± 0.01) × 10^{-6}	1.08 ± 0.01	58.9 ± 0.2
	NH_4Cl + PEG	0.228 ± 0.003	(5.97 ± 0.03) × 10^{-7}	(9.82 ± 0.01) × 10^{-7}	10.14 ± 0.06	74.0 ± 0.1
	NH_4Cl + PEG + PDADMA	0.179 ± 0.003	(2.56 ± 0.02) × 10^{-7}	(5.46 ± 0.01) × 10^{-7}	11.62 ± 0.09	74.9 ± 0.9

[a]Measured on 20 mV s^{-1} scans. [b]Calculated from peak current using the Randles−Sevcik plot with ordinary least-squares regression, errors = standard deviation (SD) of five cycles. [c]Dynamic viscosity measured by pressure drops in a flow channel, errors = SD of three measurements. [d]Bulk resistance as measured by electrochemical impedance spectroscopy (EIS), errors = SD of four measurements.

formation of ion pairs with the complementary polyelectrolyte, which we hypothesized could be put to use in slowing the rate of crossover.[34−36] Less clear before our investigation, however, was how specific combinations of active materials and polyelectrolytes in the ATPS influence the homogeneity of the electrolytes, electroreversibility of the active materials, and the formation rate and strength of the polyelectrolyte coacervate membrane, particularly at high salt concentrations, needed to minimize polarization in the device.

We found that the composition of the supporting electrolyte strongly influenced the redox reversibility of the active materials, as well as the homogeneity of the multicomponent liquid anolytes and catholytes. Initially, we examined NaCl as the supporting electrolyte salt, as most of the anionic and cationic electrolyte components are commonly synthesized and used with Na^+ and Cl^- as counterions, respectively. However, we found that the electroreversibility of ferrocyanide was poor in aqueous NaCl electrolytes (Figure S1). We resolved this using ammonium ferrocyanide in aqueous NH_4Cl (Figure 2).[32] We next investigated the influence of NH_4Cl concentration on catholyte homogeneity (Figure S2).[37] At low concentrations of NH_4Cl, PDADMA−Cl and ammonium ferrocyanide formed a precipitate, while at high concentrations of NH_4Cl, mixtures of PDADMA−Cl and PEG became cloudy. Small-angle X-ray scattering (SAXS) showed no dependence of aggregate size on the salt concentration (Figure S3). Ultimately, we showed that a concentration of 0.5 M NH_4Cl afforded good homogeneity to both anolyte and catholyte, which then allowed us to examine the influence of all components on the redox and transport properties of the liquid electrodes.

Electrolyte Characterization. To assess how the electroreversibility of methyl viologen and ferrocyanide were influenced by the increase in viscosity when dextran and PEG were present alongside charge-complementary polyelectrolytes, we performed a series of cyclic voltammetry (CV) experiments (Figure 2A,B). In the supporting electrolyte alone, both active materials underwent reversible redox reactions (Figures 2A,B, S4A,D, and S5A,B). As neither dextran nor PEG feature electrostatic charge, the introduction of either only causes the viscosity to increase, which in turn slows the diffusion of redox-active species (Table 1 and Figure S6). Upon introduction of dextran (M_r = 450 000−650 000; 15% w/v) to methyl viologen in 0.5 M NH_4Cl, the peak currents dropped slightly (Figures 2A,C and S4B), resulting in a ∼40% decrease in the diffusion coefficient of methyl viologen (Figure 2E and Table 1), as determined from a plot of peak current as a function of the square root of scan rates (eq 1 in the Methods section). The peak separation, ΔE_p, remained almost unchanged, and the half-peak potential, $E_{p/2}$, shifted by 3 mV (Figure S5A,C). Similarly, upon introduction of PEG (M_n = 20 000; 10% w/v) to ferrocyanide in 0.5 M NH_4Cl, the peak current and diffusion coefficient dropped by ∼40% (Figures 2B,D,E and S4E and Table 1). ΔE_p remained largely unchanged, while $E_{p/2}$ shifted by −21 mV (Figure S5B,D).

While viscosity played a role in modulating the electroreversibility of active materials in ATPSs containing high concentrations of electrolyte, so did the addition of polyelectrolytes with complementary charge. Specifically, when polyanionic PSS−Na (M_w = 70 000; 1% w/v) was added to methyl viologen in 15% dextran and 0.5 M NH_4Cl, the peak currents and diffusion coefficients were further reduced; especially the anodic peak current, which dropped by approximately 1 order of magnitude (Figures 2A,C,E and S4C and Table 1). The disparity in changes between anodic and cathodic peak currents reflect the different states-of-charge of the active material in the forward and reverse electrochemical reactions, which direct the electrostatic interactions in the system between the active material and the polyelectrolyte, and, therefore, the structure of the supramolecular redoxmer and its interaction with the current collector during electron transfer. Meanwhile, both ΔE_p and $E_{p/2}$ increased slightly (Figure S5A,C). Similarly, upon introduction of polycationic PDADMA−Cl (M_w = 200 000−350 000; 1% w/v) to ammonium ferrocyanide in 10% PEG and 0.5 M NH_4Cl, the peak current and diffusion coefficient were also lowered (Figures 2B,D,E and S4E and Table 1). The cathodic peak current dropped by ∼60%, while the anodic peak currents dropped by ∼40%. Meanwhile, ΔE_p also increased slightly, while $E_{p/2}$ dropped by 49 mV (Figure S5B,D). Therefore, while dextran and PEG impact electroreversibility and self-diffusion of the active materials due to the increase in viscosity, this behavior, along with the electrostatic interactions between charge-complementary polyelectrolytes and actives, are compounded in their influence on those characteristics. We find that electrochemistry is remarkably precise in revealing and quantifying the impact of the state-of-charge-dependent supramolecular (i.e., electrostatic) interactions between polyelectrolytes and the active materials on charge transfer processes between these supramolecular redoxmers and the electrodes. Despite changes in the diffusivities of the active materials, the polymers had little influence on the bulk ionic conductivity (Table 1 and Figures S6 and S7). Membrane formation and stability are critically important when fabricating structured-liquid devices. When fabricating structured-liquid batteries, high concentrations of salt relative to the active materials in the electrolyte are needed to minimize cell polarization during charge and discharge. Yet, membrane formation from polyelectrolytes at a liquid−liquid interface is known to be inhibited by salt.[37] We confirmed this by showing

https://doi.org/10.1021/jacs.1c12417
J. Am. Chem. Soc. 2022, 144, 3979−3988

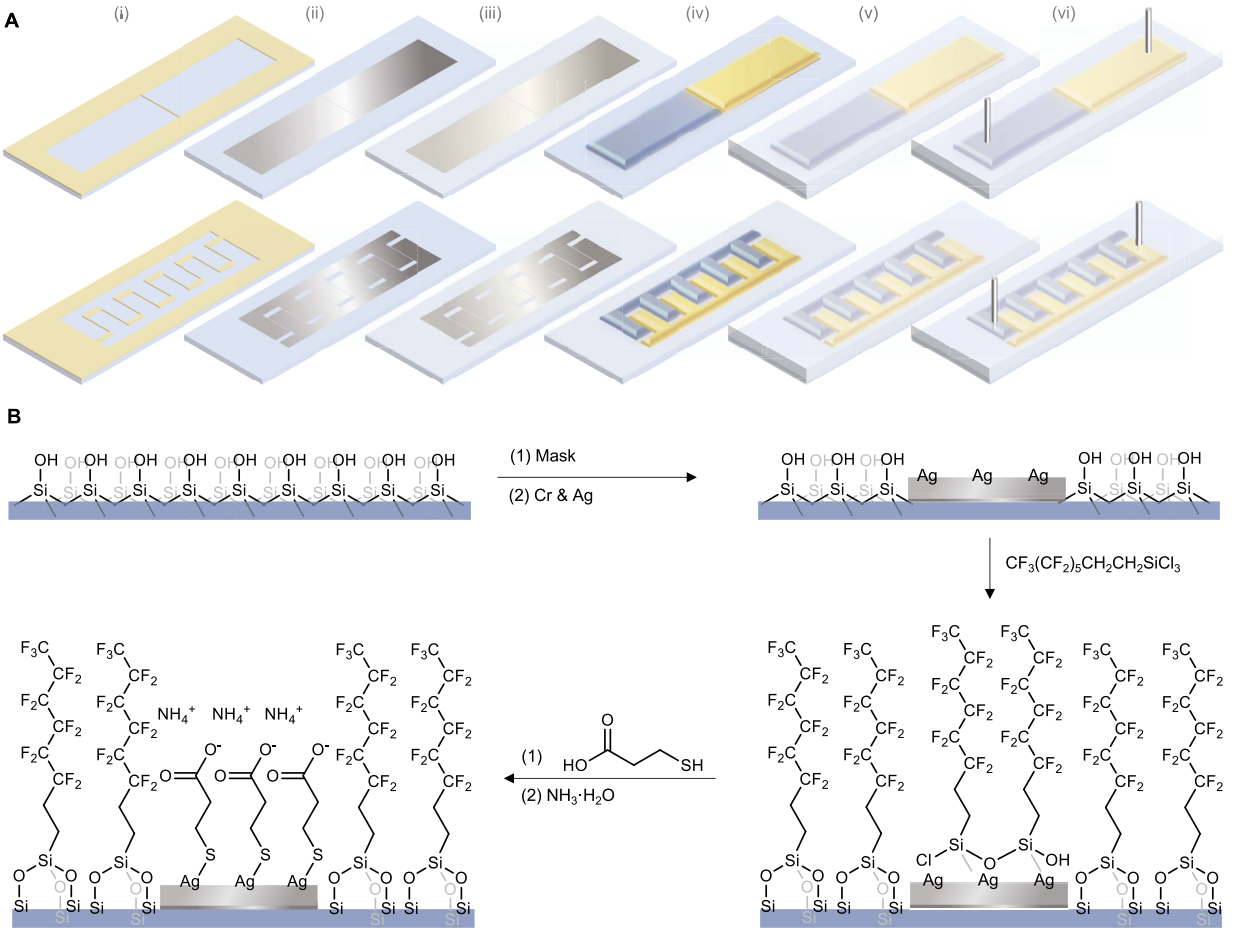

Figure 3. (A) Surface patterning and device fabrication of structured-liquid batteries. Here, an overlayer of oil slows the rate of evaporation of water, allowing the device to be cycled for hundreds of hours. (i) Masking with inscribed polyimide tape; (ii) chromium/silver deposition; (iii) surface treatment to make silver surfaces hydrophilic and glass surfaces hydrophobic; (iv) electrode printing to the confined patterns using two immiscible aqueous electrolytes containing dextran/MV/PSS (blue) and PEG/ferrocyanide/PDADMA (yellow); (v) encapsulation of the electrochemical cell under silicone oil; and (vi) wiring up the device with Ag wires as current collectors and introduction of the active materials. Both interdigitated array and parallel block configurations are shown and were tested. (B) Evolution of the surface chemistry through fabrication steps (ii) and (iii).

that PSS−PDADMA films do not form instantaneously at a water−water interface at high salt concentrations.[19] We considered alternatives, including a PSS−poly(allylamine) coacervate film, whose formation has been shown to be less sensitive to high salt concentration.[38] However, we found that the primary amines of poly(allylamine) were redox-active, forming imines at oxidizing potentials. We then considered whether PSS−PDADMA coacervate films could form at high salt concentrations.[39,40] We constructed a bulk prototype of all-aqueous biphasic electrochemical cell to study the rate of coacervate membrane formation over time and tested its stability. After 24−48 h, we found that the coacervate membrane was visible and capable of limiting diffusion of methyl viologen radical cations (Figure S8A), confirming membrane formation. After 4 days, the membrane was sufficiently strong to hold 10 mL of aqueous solution upon inversion of the crude bilayer cell (Figure S8B). This indicated that while the high salt concentration in the electrodes slows the formation of the membrane,[41] once formed, it is strong and can support the device structure indefinitely. These data also indicated that cell fabrication must take into account the rate of membrane formation prior to the introduction of the active materials to take maximum benefit of membrane blocking. We also found that the membrane added only a small contribution (~6 Ω) to the overall resistance of the cell (Figure S8C).

Cell Fabrication. Having established an understanding of the formulation of anolytes and catholytes to enable redox reversibility, active material complexation to the endogenous polyelectrolytes through ion pairing, and coacervate membrane formation at the liquid−liquid interface from charge-complementary polyelectrolytes, we next sought to implement the all-aqueous biphasic liquid electrodes in patterned and printed electrochemical devices (Figure 3). To do so, we designed a fabrication strategy for depositing current collectors on a glass slide, where the current collectors were rendered hydrophilic, while the surrounding glass surface was made hydrophobic. This wetting condition ensured that the printed electrodes were confined to the boundaries set by the current collector. We tested two types of patterned current collectors: parallel plates and interdigitated arrays (Figure S9). We thermally

https://doi.org/10.1021/jacs.1c12417
J. Am. Chem. Soc. 2022, 144, 3979−3988

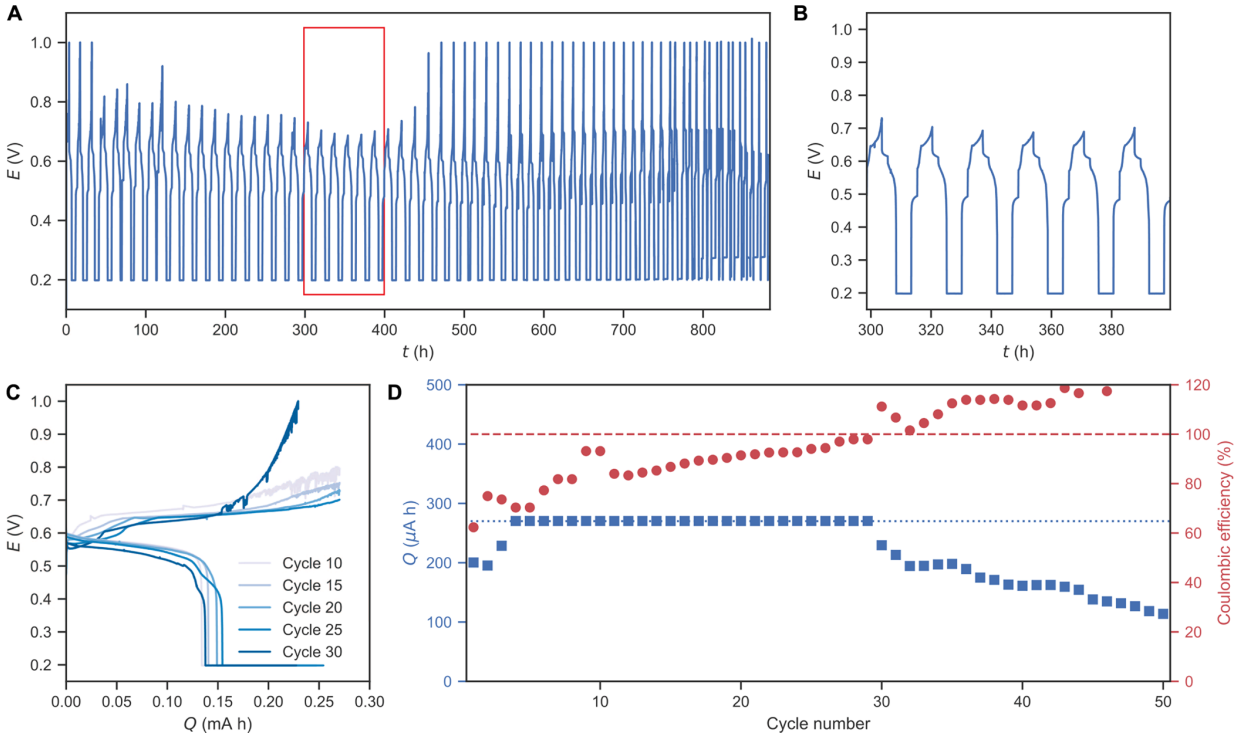

Figure 4. (A) Full cell charge/discharge curves for an under-oil all-aqueous electrochemical cell. (B) Excerpt of cycles 20−25 (indicated as a red box in Panel A). (C) Potential vs capacity in cycles 10, 20, 30, 40, and 50. (D) Accessed capacity and Coulombic efficiency of each cycle. The red dashed line indicates 100% efficiency. The blue dotted line indicates 10% state of charge. In each cycle, the cell was charged/discharged at a constant current of 54 μA with potential limits of 1.0 and 0.2 V, respectively, or up to 5 h. A constant voltage discharge for up to 5 h with a cutoff current of 3 μA. After charge/discharge, the cell was rested for 2 h.

evaporated metallic silver onto the glass surface, using chromium as the adhesion layer (Figure S10).[42] We then applied a perfluoroalkyl trichlorosilane monolayer to the entire substrate. To displace the perfluoroalkyl monolayer on silver, we introduced mercaptopropionic acid, which forms stronger bonds to the surface via thiolate linkages. We then neutralized the acid using an aqueous ammonia solution (Figure 3B). By this method, we produced superhydrophobic glass surfaces on which patterned silver current collectors are hydrophilic and salt-matched to the electrolyte used in the devices.

We found that the efficacy of electrode wetting with either of the aqueous biphasic electrolytes depended strongly on the geometry of the patterned electrode. Initially, an interdigitated array with prototypical thin fingers connected to two large reservoirs was used (Figure S11). However, the Laplace pressure drove the liquids from the fingers to the reservoirs.[21,22] Consequently, an interdigitated array with thick fingers was designed and fabricated (Figure S9B). The two electrode designs shared a similar surface area (8.04 vs 7.97 cm^2), but the boundaries between the current collectors were different (12.7 vs 120 mm). Therefore, the interface-to-volume ratios were distinct as well (0.158 vs 1.51 cm^{-1}), which translated into a difference in the areal density of polyelectrolytes (63 vs 6.6 mg cm^{-2}) and accessible membrane thickness. By increasing the volume of the anolyte and catholyte applied to the electrodes, we were able to confidently establish the interface between them, which initiated membrane formation. We found that the self-forming membrane impeded mass transfer between the two phases, as shown by the dark blue methyl viologen radical cations in Figure 1B.[19] For such a system with a thin layer of aqueous solutions, water evaporation is expected to be rapid, despite the polymer contents (eq 2 in the Methods section).[43] To limit the extent of evaporation, we implemented a simple "under-oil" approach, covering the entire device with a layer of silicone oil with a viscosity of 10 cSt.[44,45]

Structured-Liquid Battery Testing. Having established the means to pattern and print all-aqueous biphasic devices with self-forming polyelectrolyte-based coacervate membranes and ensure the longevity of the device by controlling the rate of evaporation of water, we then demonstrated that the device could be driven in and out of chemical equilibrium by the application of an electrochemical potential, where current flowed through an external circuit as the active materials in the anolyte and catholyte were charged and discharged. We galvanostatically cycled a device featuring parallel electrodes at a C/50 rate (54 μA) for 884 h (Figure 4A). In each cycle, we used a constant current charge and a constant current−constant voltage (CCCV) discharge to access the full capacity of the electrodes (Figure 4C). The charge and discharge curves plateaued at ∼0.65 and ∼0.55 V, respectively (Figure 4B,C), lower than the $E_{p/2}$ difference of 0.78 V (Figure 2E and Table 1), suggesting a potential drop at the interface of the current collector with the liquid electrodes.[46] Despite this, the device accessed 10% of its theoretical capacity (cf. Supporting Information) within four cycles and was stable for 430 h. Due to the formation of ion−polyelectrolyte complexes, vide supra, diffusion of active materials was considerably slower in

https://doi.org/10.1021/jacs.1c12417
J. Am. Chem. Soc. 2022, 144, 3979−3988

this cell. Consequently, only a fraction of the active materials in the proximity of the current collector was initially charged; however, diffusion of supramolecular redoxmer complexes and self-exchange of electrons allowed active materials farther away from the current collector to undergo redox reactions (Figure S12). During the discharge process, supramolecular redoxmers close to the current collectors were quickly discharged, leading to a rapid decrease in voltage when approximately half of the capacity was discharged. Nevertheless, most of the remaining capacity was still accessible over time with a constant voltage discharge at 0.2 V by diffusion and self-exchange (Figure 4C). The cell showed a relatively low Coulombic efficiency, which gradually increased over time (Figure 4D) as a result of a slow accumulation of charged species in the cell, likely due to slow rates of diffusion and self-exchange in the electrolyte.

Beginning with the 30th cycle, the capacity began to decrease. During this time, the Coulombic efficiency increased above 100%, which is generally indicative of side reactions. Indeed, beginning in the 25th cycle, discharge curves showed a secondary plateau consistent with a new species undergoing reduction (Figure 4C). This new feature in the discharge curves may arise from redox-active species in the wrong electrode compartment resulting from crossover evident when operating the device over long periods of time. Notably, the association of active materials with charge-complementary polyelectrolytes is in dynamic equilibrium. This equilibrium is influenced by the state of charge of the electrode, as ion-pairing strength will depend on the redox state of the active material. If at a specific state of charge, the strength of ion pairing is low and ion-separated pairs are more prevalent, this could lead to increased rates of crossover as the effective size of the redox-active species is that of the small molecule and no longer that of the much larger supramolecule. Alternatively, the capacity fade may be tied to slow but cumulative effects of evaporation from the electrodes due to the water permeability of polydimethylsiloxane.[45] In comparison to the parallel plate electrode geometry, devices featuring interdigitated array electrodes showed significantly poorer cyclability, likely due to the larger interfacial area and thinner membrane—both of which influence the rate of crossover (Figures S13 and S14 as well as Figure 1B). In addition, a reference cell without polyelectrolytes in the parallel plate geometry showed no indication of sustainable cycling (Figure S15). In this way, we reasoned that crossover, rather than evaporation, was the most likely explanation for the observed capacity fade.

To confirm this, we quantified the extent of crossover by measuring the concentrations of active materials in each phase (Figure 5). After siphoning off the silicone oil, we retrieved the cell and allowed the water to evaporate, leaving behind the films of polymer, salt, and actives on each of the current collectors. We carefully retrieved the contents from each phase, diluting them in 0.5 M NH_4Cl prior to analysis by CV (Figure S16). The methyl viologen concentration in the PEG phase and the ferrocyanide concentration in the dextran phase were then measured electrochemically against calibration curves using the cathodic peak current of methyl viologen and the anodic peak current of ferrocyanide to avoid interference from oxygen/hydrogen evolution reactions. We found that ~12% of methyl viologen and ~20% of ferrocyanide diffused across the coacervate membrane after 24 h of annealing and 884 h of cycling. Thus, up to 20% of the capacity fade observed during this period can be attributed to crossover, whereas other

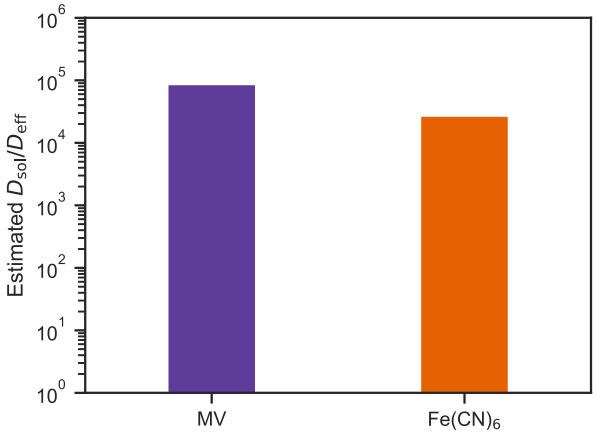

Figure 5. Estimated membrane-blocking ability reported as a blocking ratio, D_{sol}/D_{eff}. Here, D_{sol} is the diffusion of the active material in the electrolyte and D_{eff} is the effective diffusion of the active material through the coacervate membrane.

phenomena, including increased polarization due to water evaporation, are responsible for the rest.

With these data, we estimated the membrane-blocking ability. To calculate the diffusive permeability of each active material across the PSS−PDADMA coacervate membrane, D_{eff}, requires that the initial and permeated concentration of active materials is known alongside the total electrolyte volume, the total time during which the actives were in contact with the membrane, as well as the surface area and thickness of the membrane (eq 3 in the Methods section).[31] While these variables are known or were determined, the thickness of the membrane was difficult to measure, as it self-forms with a relatively small area at a liquid−liquid interface at an orientation that is normal to the plane of the underlying substrate. Elsewhere, the thickness of PSS−PDADMA coacervate films assembled layer-by-layer at a salt concentration of 0.5 M reached up to 500 nm for 30 layers.[47,48] In the absence of the layer-by-layer technique, PSS−PDADMA coacervate membranes are not usually as thick:[19] scanning electron micrographs of a PSS−PDADMA assembly, similar to the one explored here, were only a few hundred nanometers thick.[49] Even if we assume that the PSS−PDADMA membrane was 500 nm thick, D_{eff} can be no more than 5.8×10^{-12} and 9.6×10^{-12} cm^2 s^{-1} for methyl viologen and ferrocyanide, respectively. Therefore, the membrane-blocking ability, D_{sol}/D_{eff}, for methyl viologen and ferrocyanide was estimated to be at least 8.7×10^4 and 2.7×10^4, respectively; D_{sol} values were taken from polyelectrolyte complexes of the uncharged species taken in either dextran or PEG aqueous electrolyte phases (Table 1). This is remarkable in that values of $D_{sol}/D_{eff} > 10^4$ are rare for membranes and small-molecule active materials, more often requiring conformationally rigid microporous and nanoporous polymer membranes, whose voids are on the same length scale as the solvated actives.[7,34] Careful screening of redox-active species and polyelectrolytes for a more robust binding may further mitigate crossover and improve the cycling stability of structured-liquid batteries

■ CONCLUSIONS

Our results demonstrate that it is now possible to precisely define the electrochemical potential in compartmentalized

https://doi.org/10.1021/jacs.1c12417
J. Am. Chem. Soc. 2022, 144, 3979−3988

chemical systems comprising multiphasic liquids that are printed or patterned in arbitrary shapes and forms, provided they meet at an interface. We are able to maintain such systems far from chemical equilibrium by controlling the rates of mass transfer between the two liquid phases. We achieved this by increasing the effective size of the active materials through ion pairing with charge-complementary polyelectrolytes and by blocking the crossover of these supramolecular redoxmers with polyelectrolyte coacervate membranes that self-form at the interface between the liquid phases. In the absence of such control, the stored chemical energy would normally be dissipated internally through cross-annihilation via redox reactions. With this control, it becomes possible to harness the stored chemical energy to perform useful work, e.g., powering a load on an external circuit as the structured-liquid battery is discharged. This behavior, which has been realized here in an artificial synthetic system with broad tunability, is reminiscent of biological systems that stay out of equilibrium by compartmentalizing function in both membrane-bound and membrane-less organelles, allowing them to adapt and respond to local chemical and environmental cues as well as various physical stimuli. We further see intriguing opportunities to understand and control coacervate membrane assembly and reconfigurability using well-controlled ion fluxes at liquid−liquid interfaces, as is possible with structured-liquid batteries.[50−56]

METHODS

Materials. Dextran from *Leuconostoc* spp. (Sigma-Aldrich, M_r 450 000−650 000), poly(ethylene glycol) (PEG, Aldrich, M_n 20 000), sodium ferrocyanide decahydrate ($Na_4Fe(CN)_6{\cdot}10H_2O$, Sigma-Aldrich, 99%), methyl viologen dichloride hydrate (MV, Sigma-Aldrich, 98%), poly(sodium 4-styrenesulfonate) (PSS−Na, Sigma-Aldrich, M_w 70 000), poly(diallyldimethylammonium chloride) (PDADMA−Cl, Sigma-Aldrich, M_w 200 000−350 000), ammonium chloride (NH_4Cl, Sigma-Aldrich, 99.5%), trichloro(1*H*,1*H*,2*H*,2*H*-perfluoro)octylsilane (PFOTS, Sigma-Aldrich, 97%), 3-mercaptopropionic acid (Sigma-Aldrich, 99%), hexanes (EMD, 99.9%), and silicone oil (Sigma-Aldrich, 10 cSt) were used without further purification. Typically, 18.2 MΩ water was obtained from a Millipore Milli-Q water purification system. Ammonium ferrocyanide heptahydrate ($(NH)_4Fe(CN)_6{\cdot}7H_2O$) was prepared according to a literature procedure.[32]

Instrumentation. All electrochemistry experiments were performed using a BioLogic VMP3 potentiostat inside a VAC OMNI-LAB glovebox filled with nitrogen.

Cyclic Voltammetry. Six aqueous solutions were prepared: (a) 10 mg mL^{-1} $Na_4Fe(CN)_6{\cdot}10H_2O$ and 0.5 M NH_4Cl; (b) 100 mg mL^{-1} PEG, 10 mg mL^{-1} $Na_4Fe(CN)_6{\cdot}10H_2O$, and 0.5 M NH_4Cl; (c) 100 mg mL^{-1} PEG, 10 mg mL^{-1} PDADMAC, 10 mg mL^{-1} $Na_4Fe(CN)_6{\cdot}10H_2O$, and 0.5 M NH_4Cl; (d) 10 mg mL^{-1} MV and 0.5 M NH_4Cl; (e) 150 mg mL^{-1} dextran, 10 mg mL^{-1} (w/v) MV, and 0.5 M NH_4Cl; and (f) 150 mg mL^{-1} dextran, 10 mg mL^{-1} PSS, 10 mg mL^{-1} MV, and 0.5 M NH_4Cl. A 3-mm glassy carbon electrode was used as the working electrode. A Pt wire was used as the counter electrode. A AgCl/Ag in 3.0 M NaCl electrode was used as the reference electrode. Cyclic voltammetry with scan rates of 10, 20, 50, 100, and 200 mV s^{-1} was performed to each of the solutions. The diffusion coefficients of the active materials were evaluated by plotting peak current vs scan rate based on Randles−Sevcik equation

$$i_p = 0.4463nFAc\left(\frac{nFvD}{RT}\right)^{1/2} \quad (1)$$

where i_p is the peak current of cyclic voltammetry in A, n is the number of electrons transferred in the redox event, A is the electrode area in cm^2, F is the Faraday constant in C mol^{-1}, D is the diffusion coefficient in cm^2 s^{-1}, C is the concentration of the active material in mol cm^{-3}, v is the scan rate in V s^{-1}, R is the universal gas constant in J K^{-1} mol^{-1}, and T is the temperature in K.

Small-Angle X-ray Scattering (SAXS). The SAXS measurements were performed on a Xenocs Xeuss 2.0 SAXS instrument equipped with a Pilatus 3 detector, in which the camera length was 6400 mm and the X-ray wavelength was 0.154189 nm when the sample solutions were sandwiched between two polyimide films with a 1.0 mm thick Teflon spacer. Each sample was exposed for 3600 s. Aqueous solutions containing PEG, ammonium chloride, and sodium ferrocyanide were prepared before the experiment. Shortly before SAXS measurement of each sample, 20% PDADMA−Cl solutions were mixed with the aforementioned solution. The mixture was shaken vigorously before being injected into the empty Teflon holders through one of two 0.75 mm openings. The final concentrations of the components were 100 mg mL^{-1} PEG, 0.2 M $Fe(CN)_6^{4-}$, 10 mg mL^{-1} PDADMA−Cl, and 0−1.0 M NH_4Cl. The acquired data was processed with FIT2D 18 (Beta)software.[57]

Bulk Prototype of All-Aqueous Biphasic Batteries. In a glovebox filled with nitrogen, two 3 mm glassy carbon electrodes were installed onto a custom-made electrochemical cell (Figure S3a). A 10 mL of aqueous solution containing 15% (w/v) dextran, 1% (w/v) PSS−Na, and 0.5 M NH_4Cl was added to the bottom. Another 10 mL of aqueous solution containing 10% (w/v) PEG, 1% (w/v) PDADMA−Cl, and 0.5 M NH_4Cl was added carefully on the top of the first solution. The biphasic mixture was allowed to age overnight. Typically, 0.5 mL of the solution was carefully withdrawn from the bottom phase and used to dissolve 51.4 mg (0.2 mmol) of MV. The solution was injected back to the bottom phase. One milliliter of the solution was taken from the top phase and used to dissolve 96.8 mg (0.2 mmol) of $Na_4Fe(CN)_6{\cdot}10H_2O$. The solution was added slowly back to the top phase. The biphasic mixture was allowed to equilibrate overnight again. The battery was charged/discharged between 1 and 0 V.

Preparation of Current Collectors. Micro slides (VWR, nominal 1″ × 3″) were cleaned using UV-ozone for 20 min and covered by polyimide tape. The tape was carved into the designed shape (Figure S8) using a razor blade. A 5 nm layer of Cr and a 100 nm layer of Ag were deposited sequentially on the exposed surface using a thermal evaporator at 0.05−0.1 and 0.2−0.5 nm s^{-1}, respectively. The metal coating was aged for at least 24 h. The polyimide tape was carefully removed after being rinsed by chloroform. The slides were flipped and immersed in 0.1% PFOTS in hexanes for 1 min. The treated slides were rinsed extensively with acetone. After the slides became dry, a 1% 3-mercaptopropionic acid aqueous solution was deposited on top of the Ag surface. After the slides stood for 1 min, the aqueous solution was removed. The treated surface was washed extensively with water. Then, a 1% ammonia solution was used to neutralize the surface. The unreacted ammonia was rinsed away with water and let dry.

Resistance Measurements. Resistance of the cells or solutions was measured by electrochemical impedance spectra from 200 kHz to 0.1 Hz with 100 mV sinus amplitude.

Viscosity Measurements. Viscosities of the solutions were measured with a RheoSense microVISC viscometer with A05 cartridge. Measurements were taken at 22 °C.

Fabrication of Structured-Liquid Batteries. A treated glass slide with current collectors was transferred into a glovebox and placed inside a 30 mm × 76 mm rectangular glass dish. The glass dish was placed inside a plastic container with two holes in the lid. Two open vials of water were placed inside the container to create a moist environment. An aqueous solution containing 100 mg mL^{-1} PEG, 10 mg mL^{-1} PDADMA−Cl, and 0.5 M NH_4Cl was added slowly to one current collector. Another aqueous solution containing 150 mg mL^{-1} dextran, 10 mg mL^{-1} PSS−Na, and 0.5 M NH_4Cl was added simultaneously to the other current collector. The two solutions were added until they merged on the gap between the two current collectors. Typically, 0.45 mL of each of the solutions was consumed. Silicone oil was added on the top of aqueous solutions until the aqueous phase was thoroughly immersed. The two current collectors

https://doi.org/10.1021/jacs.1c12417
J. Am. Chem. Soc. 2022, 144, 3979−3988

were, respectively, connected to the working electrode and counter/reference electrode clamps using silver rods. The polyelectrolyte solutions were allowed to age overnight. $(NH_4)_4Fe(CN)_6{\cdot}7H_2O$ and MV were dissolved in the aforementioned PEG solution and dextran solution, respectively, and added carefully to their corresponding phases to make the final concentration of active materials in each phase at 0.2 M. The active materials were allowed to diffuse for 24 h before charge and discharge. The theoretical capacity of the cell was calculated by $C_{theo} = FcV = 2.7$ mA h, where F is Faraday constant, c is the molar concentration of the active species, and V is the electrolyte volume.

Estimation of Water Evaporation Rate. Previous literature showed that a similar system containing dextran and PEG had little difference in water loss rate in comparison to pure water.[43] Therefore, we can estimate the water loss rate without any evaporation mitigation based on pure water and Langmuir's equation for evaporation.

$$\frac{dm}{dt} = A(p_v - p_p)\sqrt{\frac{M}{2\pi RT}} \quad (2)$$

To simplify the estimation, we assume that the environment inside our glovebox is 20 °C with 1.0 in Hg overpressure and a high water content of 2.0% (RH ~ 90%). For the parallel block cell, the surface area, $A = 8.04 \times 10^{-4}$ m^2; the saturated water vapor pressure, $p_v = 2.34 \times 10^3$ Pa; the water partial pressure, $p_p = 2.09 \times 10^3$ Pa; the water molar mass, $M = 0.0180$ kg mol^{-1}; the gas constant, $R = 8.314$ J K^{-1} mol^{-1}; and the temperature $T = 293$ K. Therefore, the water loss rate, dm/dt, can be estimated to be 2.18×10^{-5} kg s^{-1}, which translates to a complete water loss at roughly 500 s. This highlights the necessity of an under-oil approach for long-term device operation.

Structured-Liquid Cell Cycling. Under-oil all-liquid electrochemical cells were charged galvanostatically until a potential limit of 1.0 V or until the theoretical capacity was reached, after which the cells were allowed to rest for 2 h. They were then discharged galvanostatically until a potential limit of 0.2 V. A constant voltage discharge at 0.2 V was applied until the current dropped below 3 μA. The cells were subsequently allowed to rest for 2 h before initiating the next cycle.

Analysis of Active-Material Crossover. After cell cycling, the silicone oil was removed from the cell holder. The all-aqueous cell turned into a piece of thin, soft film within 15 min. The film was peeled off completely from the current collectors and cut at the interface of the two phases. Each of the two phases was diluted with 0.5 M NH_4Cl in volumetric flasks to 5.0 mL. Cyclic voltammetry was used to measure the concentration of MV in the PEG phase and ferrocyanide in the dextran phase. Calibration curves were established by adding MV into the PEG phase and ferrocyanide into the dextran phase. To make the PEG phase, 41.0 mg of $(NH)_4Fe(CN)_6{\cdot}7H_2O$, 134 mg of NH_4Cl, 6.0 mg/30 μL of PDADMA−Cl 20% solution, and 60 mg of PEG were diluted to 5.0 mL. To make the dextran phase, 25.7 mg of MV, 134 mg of NH_4Cl, 6.0 mg of PSS−Na, and 90 mg of dextran were diluted to 5.0 mL. Typically, 12.8 mg of MV was dissolved in 25 μL of the PEG phase and added into the remaining PEG phase in 2.5 μL of increments corresponding to 5.2, 10.4, 15.5, 20.6, 25.6, 30.6, 35.5, 40.4, and 45.2% crossover of MV. Typically, 20.5 mg of $(NH)_4Fe(CN)_6{\cdot}7H_2O$ was dissolved in 25 μL of the dextran phase and added into the remaining dextran phase in 2.5 μL of increments corresponding to 5.2, 10.4, 15.5, 20.6, 25.6, 30.6, 35.5, 40.4, and 45.2% crossover of ferrocyanide.

Calculation of the Effective Diffusion Coefficient across the Membrane. The effective diffusion coefficient, D_{eff}, was calculated based on our previously reported analytical method[34]

$$D_{eff} = \frac{C_{perm}(t)lV}{C_0At} \quad (3)$$

where C_{perm} and $C_0 = 0.2$ M are the permeated and initial concentrations of the active materials, respectively, l is the thickness of the coacervate membrane, $V = 0.5$ cm^3 is the volume of the electrolyte, $A = 0.16$ cm^2 is the surface area of the membrane, and $t = 3.27 \times 10^6$ s is the time between addition of active materials and disassembly of the cell. C_{perm}/C_0 was measured by postmortem cyclic voltammetry, vide supra.

■ ASSOCIATED CONTENT

Supporting Information

The Supporting Information is available free of charge at https://pubs.acs.org/doi/10.1021/jacs.1c12417.

Cyclic voltammetry data, photographs of electrolytes and experimental setups, electrolyte characterization data, Nyquist plots, technical drawings, cell performance for controls, crossover calibration curves, and data used in the analysis of diffusive permeability of the actives through the coacervate membrane (PDF)

■ AUTHOR INFORMATION

Corresponding Author

Brett A. Helms − *Materials Sciences Division, Lawrence Berkeley National Laboratory, Berkeley, California 94720, United States; The Molecular Foundry, Lawrence Berkeley National Laboratory, Berkeley, California 94720, United States;* orcid.org/0000-0003-3925-4174; Email: bahelms@lbl.gov

Authors

Jiajun Yan − *Materials Sciences Division, Lawrence Berkeley National Laboratory, Berkeley, California 94720, United States; School of Physical Science and Technology, ShanghaiTech University, Shanghai 201210, China;* orcid.org/0000-0003-3286-3268

Michael A. Baird − *Department of Chemistry, University of California, Berkeley, California 94720, United States*

Derek C. Popple − *Department of Chemistry, University of California, Berkeley, California 94720, United States; Department of Physics, University of California, Berkeley, California 94720, United States*

Alex Zettl − *Materials Sciences Division, Lawrence Berkeley National Laboratory, Berkeley, California 94720, United States; Department of Physics, University of California, Berkeley, California 94720, United States; Kavli Energy NanoScience Institute at the University of California Berkeley and the Lawrence Berkeley National Laboratory, Berkeley, California 94720, United States*

Thomas P. Russell − *Materials Sciences Division, Lawrence Berkeley National Laboratory, Berkeley, California 94720, United States; Polymer Science and Engineering Department, University of Massachusetts, Conte Center for Polymer Research, Amherst, Massachusetts 01003, United States*

Complete contact information is available at: https://pubs.acs.org/10.1021/jacs.1c12417

Author Contributions

The manuscript was written through the contributions of all authors. All authors have given approval to the final version of the manuscript.

Notes

The authors declare no competing financial interest.

■ ACKNOWLEDGMENTS

This work was supported primarily by the U.S. Department of Energy, Office of Science, Office of Basic Energy Sciences, Materials Sciences and Engineering Division under contract

no. DE-AC02-05-CH11231 within the Adaptive Interfacial Assemblies Toward Structuring Liquids program (KCTR16). Portions of the work—specifically, synthesis and characterization of the active materials—were carried out at the Molecular Foundry, which is supported by the Office of Science, Office of Basic Energy Sciences, of the U.S. Department of Energy under Contract No. DE-AC02-05-CH11231. M.A.B. was supported by the Advanced Research Projects Agency–Energy Integration and Optimization of Novel Ion Conducting Solids (IONICS) program under grant no. DE-AR0000774. The SAXS experiment was supported by a start-up grant to J.Y. at ShanghaiTech University. The authors thank Ganhua Xie, Miranda Baran, Sung-Ju Cho, Paul Ashby, Zhiqiang Zou, and Zhi Qiao for useful discussions.

■ ABBREVIATIONS

PDADMA–Cl	poly(diallyldimethylammonium chloride)
PSS–Na	poly(sodium 4-styrenesulfonate)
ATPS	aqueous two-phase system
PEG	poly(ethylene glycol)
SHE	standard hydrogen electrode
CV	cyclic voltammetry

■ REFERENCES

(1) Bradwell, D. J.; Kim, H.; Sirk, A. H. C.; Sadoway, D. R. Magnesium–antimony liquid metal battery for stationary energy storage. *J. Am. Chem. Soc.* **2012**, *134*, 1895–1897.
(2) Wang, K.; et al. Lithium–antimony–lead liquid metal battery for grid-level energy storage. *Nature* **2014**, *514*, 348–350.
(3) Ding, Y.; et al. Room-temperature all-liquid-metal batteries based on fusible alloys with regulated interfacial chemistry and wetting. *Adv. Mater.* **2020**, *32*, No. 2002577.
(4) Ding, Y.; Guo, X.; Qian, Y.; Yu, G. Low-temperature multielement fusible alloy-based molten sodium batteries for grid-scale energy storage. *ACS Cent. Sci.* **2020**, *6*, 2287–2293.
(5) Gao, H.; Zhou, W.; Park, K.; Goodenough, J. B. A sodium-ion battery with a low-cost cross-linked gel-polymer electrolyte. *Adv. Energy Mater.* **2016**, *6*, No. 1600467.
(6) Li, S.; et al. A semiliquid lithium metal anode. *Joule* **2019**, *3*, 1637–1646.
(7) Baran, M. J.; et al. Design rules for membranes from polymers of intrinsic microporosity for crossover-free aqueous electrochemical devices. *Joule* **2019**, *3*, 2968–2985.
(8) Hendriks, K. H.; et al. High-performance oligomeric catholytes for effective macromolecular separation in nonaqueous redox flow batteries. *ACS Cent. Sci.* **2018**, *4*, 189–196.
(9) Wang, W.; et al. Recent progress in redox flow battery research and development. *Adv. Funct. Mater.* **2013**, *23*, 970–986.
(10) Braff, W. A.; Bazant, M. Z.; Buie, C. R. Membrane-less hydrogen bromine flow battery. *Nat. Commun.* **2013**, *4*, No. 2346.
(11) Cho, S.-J.; et al. Monolithic heterojunction quasi-solid-state battery electrolytes based on thermodynamically immiscible dual phases. *Energy Environ. Sci.* **2019**, *12*, 559–565.
(12) Karakurt, I. et al. In *Membraneless Microfluidic Redox Battery for Wearable Electronics Applications*, 2017 19th International Conference on Solid-State Sensors, Actuators and Microsystems (TRANSDUCERS); IEEE, 2017.
(13) Meng, J.; et al. A stirred self-stratified battery for large-scale energy storage. *Joule* **2020**, *4*, 953–966.
(14) Navalpotro, P.; Palma, J.; Anderson, M.; Marcilla, R. A membrane-free redox flow battery with two immiscible redox electrolytes. *Angew. Chem., Int. Ed.* **2017**, *56*, 12460–12465.
(15) Liu, A. J.; Nagel, S. R. Jamming is not just cool any more. *Nature* **1998**, *396*, 21–22.
(16) Cui, M.; Emrick, T.; Russell, T. P. Stabilizing liquid drops in nonequilibrium shapes by the interfacial jamming of nanoparticles. *Science* **2013**, *342*, 460–463.
(17) Feng, W.; et al. Harnessing liquid-in-liquid printing and micropatterned substrates to fabricate 3-dimensional all-liquid fluidic devices. *Nat. Commun.* **2019**, *10*, No. 1095.
(18) Forth, J.; et al. Building reconfigurable devices using complex liquid–fluid interfaces. *Adv. Mater.* **2019**, *31*, No. 1806370.
(19) Xie, G.; et al. Compartmentalized, all-aqueous flow-through-coordinated reaction systems. *Chem* **2019**, *5*, 2678–2690.
(20) Liu, X.; et al. Reconfigurable ferromagnetic liquid droplets. *Science* **2019**, *365*, 264–267.
(21) Scheiger, J. M.; et al. Liquid wells as self-healing, functional analogues to solid vessels. *Adv. Mater.* **2021**, *33*, No. 2100117.
(22) Wu, L.; Dong, Z.; Li, F.; Song, Y. Designing Laplace pressure pattern for microdroplet manipulation. *Langmuir* **2018**, *34*, 639–645.
(23) Wang, Q.; Schlenoff, J. B. The polyelectrolyte complex/coacervate continuum. *Macromolecules* **2014**, *47*, 3108–3116.
(24) Darling, R.; Gallagher, K.; Xie, W.; Su, L.; Brushett, F. Transport property requirements for flow battery separators. *J. Electrochem. Soc.* **2016**, *163*, A5029.
(25) grosse Austing, J.; Kirchner, C. N.; Komsiyska, L.; Wittstock, G. Investigation of crossover processes in a unitized bidirectional vanadium/air redox flow battery. *J. Power Sources* **2016**, *306*, 692–701.
(26) Knehr, K.; Agar, E.; Dennison, C.; Kalidindi, A.; Kumbur, E. A transient vanadium flow battery model incorporating vanadium crossover and water transport through the membrane. *J. Electrochem. Soc.* **2012**, *159*, A1446.
(27) Albertsson, P.-Å. Partition of proteins in liquid polymer–polymer two-phase systems. *Nature* **1958**, *182*, 709–711.
(28) Diamond, A.; Hsu, J. Phase diagrams for dextran–PEG aqueous two-phase systems at 22 C. *Biotechnol. Tech.* **1989**, *3*, 119–124.
(29) Ryden, J.; Albertsson, P.-Å. Interfacial tension of dextran—polyethylene glycol—water two—phase systems. *J. Colloid Interface Sci.* **1971**, *37*, 219–222.
(30) Hu, B.; DeBruler, C.; Rhodes, Z.; Liu, T. L. Long-cycling aqueous organic redox flow battery (AORFB) toward sustainable and safe energy storage. *J. Am. Chem. Soc.* **2017**, *139*, 1207–1214.
(31) Liu, T.; Wei, X.; Nie, Z.; Sprenkle, V.; Wang, W. A total organic aqueous redox flow battery employing a low cost and sustainable methyl viologen anolyte and 4-HO-tempo catholyte. *Adv. Energy Mater.* **2016**, *6*, No. 1501449.
(32) Luo, J.; et al. Unprecedented capacity and stability of ammonium ferrocyanide catholyte in pH neutral aqueous redox flow batteries. *Joule* **2019**, *3*, 149–163.
(33) Wei, X.; et al. An aqueous redox flow battery based on neutral alkali metal ferri/ferrocyanide and polysulfide electrolytes. *J. Electrochem. Soc.* **2016**, *163*, A5150.
(34) Doris, S. E.; et al. Macromolecular design strategies for preventing active-material crossover in non-aqueous all-organic redox-flow batteries. *Angew. Chem., Int. Ed.* **2017**, *56*, 1595–1599.
(35) Lai, Y. Y.; Li, X.; Zhu, Y. Polymeric active materials for redox flow battery application. *ACS Appl. Polym. Mater.* **2020**, *2*, 113–128.
(36) Manning, G. S. Limiting laws and counterion condensation in polyelectrolyte solutions I. Colligative properties. *J. Chem. Phys.* **1969**, *51*, 924–933.
(37) Chollakup, R.; Beck, J. B.; Dirnberger, K.; Tirrell, M.; Eisenbach, C. D. Polyelectrolyte molecular weight and salt effects on the phase behavior and coacervation of aqueous solutions of poly(acrylic acid) sodium salt and poly(allylamine) hydrochloride. *Macromolecules* **2013**, *46*, 2376–2390.
(38) Chollakup, R.; Smitthipong, W.; Eisenbach, C. D.; Tirrell, M. Phase behavior and coacervation of aqueous poly(acrylic acid)–poly(allylamine) solutions. *Macromolecules* **2010**, *43*, 2518–2528.
(39) Dubas, S. T.; Schlenoff, J. B. Factors controlling the growth of polyelectrolyte multilayers. *Macromolecules* **1999**, *32*, 8153–8160.
(40) Qin, J.; et al. Interfacial tension of polyelectrolyte complex coacervate phases. *ACS Macro Lett.* **2014**, *3*, 565–568.

https://doi.org/10.1021/jacs.1c12417
J. Am. Chem. Soc. 2022, 144, 3979–3988

(41) Tang, K.; Besseling, N. A. M. Formation of polyelectrolyte multilayers: ionic strengths and growth regimes. *Soft Matter* **2016**, *12*, 1032−1040.
(42) Benjamin, P.; Weaver, C. The adhesion of evaporated metal films on glass. *Proc. R. Soc. London, Ser. A* **1962**, *261*, 516−531.
(43) Guo, W.; et al. Non-associative phase separation in an evaporating droplet as a model for prebiotic compartmentalization. *Nat. Commun.* **2021**, *12*, No. 3194.
(44) Li, C.; et al. Under oil open-channel microfluidics empowered by exclusive liquid repellency. *Sci. Adv.* **2020**, *6*, No. aay9919.
(45) Robb, W. Thin silicone membranes, their permeabilities and uses. *Ann. N. Y. Acad. Sci.* **1968**, *146*, 119−137.
(46) Verwey, E. J. W.; Niessen, K. F. XL. The electrical double layer at the interface of two liquids. *London, Edinburgh Dublin Philos. Mag. J. Sci.* **1939**, *28*, 435−446.
(47) Guzmán, E.; Ritacco, H.; Rubio, J. E.; Rubio, R. G.; Ortega, F. Salt-induced changes in the growth of polyelectrolyte layers of poly(diallyl-dimethylammonium chloride) and poly(4-styrene sulfonate of sodium). *Soft Matter* **2009**, *5*, 2130−2142.
(48) Iturri Ramos, J. J.; Stahl, S.; Richter, R. P.; Moya, S. E. Water content and buildup of poly(diallyldimethylammonium chloride)/poly(sodium 4-styrenesulfonate) and poly(allylamine hydrochloride)/poly(sodium 4-styrenesulfonate) polyelectrolyte multilayers studied by an in situ combination of a quartz crystal microbalance with dissipation monitoring and spectroscopic ellipsometry. *Macromolecules* **2010**, *43*, 9063−9070.
(49) Xie, G.; et al. Hanging droplets from liquid surfaces. *Proc. Natl. Acad. Sci. U.S.A.* **2020**, *117*, 8360−8365.
(50) Hyman, A. A.; Weber, C. A.; Jülicher, F. Liquid-liquid phase separation in biology. *Annu. Rev. Cell Dev. Biol.* **2014**, *30*, 39−58.
(51) Mitrea, D. M.; Kriwacki, R. W. Phase separation in biology; functional organization of a higher order. *Cell Commun. Signaling* **2016**, *14*, No. 1.
(52) Boeynaems, S.; et al. Protein phase separation: A new phase in cell biology. *Trends Cell Biol.* **2018**, *28*, 420−435.
(53) Wheeler, R. J.; Hyman, A. A. Controlling compartmentalization by non-membrane-bound organelles. *Philos. Trans. R. Soc. London, Ser. B* **2018**, *373*, No. 20170193.
(54) Wolozin, B.; Ivanov, P. Stress granules and neurodegeneration. *Nat. Rev. Neurosci.* **2019**, *20*, 649−666.
(55) Gomes, E.; Shorter, J. The molecular language of membraneless organelles. *J. Biol. Chem.* **2019**, *294*, 7115−7127.
(56) O'Flynn, B. G.; Mittag, T. The role of liquid−liquid phase separation in regulating enzyme activity. *Curr. Opin. Cell Biol.* **2021**, *69*, 70−79.
(57) Hammersley, A. P. FIT2D: a multi-purpose data reduction, analysis and visualization program. *J. Appl. Crystallogr.* **2016**, *49*, 646−652.

Recommended by ACS

Engineering Multiscale Coupled Electron/Ion Transport in Battery Electrodes
Jingxu Zheng, Lynden A. Archer, *et al.*
DECEMBER 13, 2021
ACS NANO
READ

Li^+ and Oxidant Addition To Control Ionic and Electronic Conduction in Ionic Liquid-Functionalized Conjugated Polymers
Dakota Rawlings, Rachel A. Segalman, *et al.*
AUGUST 06, 2021
CHEMISTRY OF MATERIALS
READ

Comparison of Separators vs Membranes in Nonaqueous Redox Flow Battery Electrolytes Containing Small Molecule Active Materials
Zhiming Liang, Susan A. Odom, *et al.*
MAY 24, 2021
ACS APPLIED ENERGY MATERIALS
READ

Exchange-Mediated Transport in Battery Electrolytes: Ultrafast or Ultraslow?
Bogdan Dereka, Andrei Tokmakoff, *et al.*
APRIL 26, 2022
JOURNAL OF THE AMERICAN CHEMICAL SOCIETY
READ

Get More Suggestions >

https://doi.org/10.1021/jacs.1c12417
J. Am. Chem. Soc. 2022, 144, 3979−3988